This is a preprint, the final version is subject to change, of the American Mineralogist (MSA)
Cite as Authors (Year) Title. American Mineralogist, in press.
(DOI will not work until issue is live.) DOI: http://dx.doi.org/10.2138/am-2017-5831

Revision 3

Title: Melting relations in the system $CaCO_3$-$MgCO_3$ at 6 GPa

Authors and affiliation:
Müller Jan, Koch-Müller Monika, Rhede Dieter, Franziska D.H. Wilke, Wirth Richard
GFZ, German Research Centre for Geoscience, Telegrafenberg, D-14473 Potsdam, Germany
Corresponding author: Jan Müller, jmueller@gfz-potsdam.de

Abstract

In order to define liquidus and solidus of the system $CaCO_3$-$MgCO_3$ rotating multi-anvil experiments were performed at 6 GPa in the temperature range from 1300 °C to 1800 °C under anhydrous conditions. Additionally, experiments under hydrous conditions were performed in the Mg-rich part of the phase diagram. To determine the melting point of the endmember magnesite at 6 GPa falling sphere/body experiments were performed. The run products were analyzed using electron microprobe, Raman spectroscopy and X-ray diffraction. Some of the run products were investigated by transmission electron microscopy (TEM).

Previous studies report tremendous quenching problems in melting experiments of carbonates, as the primary grown carbonates could not be distinguished from the quenched melt. With the help of rotating multi-anvil experiments the primary grown crystals could be separated from the melt phase and the compositions of both phases could be analyzed by electron microprobe. Compared to the results of static experiments the corresponding phase diagram under anhydrous conditions is significantly different. The anhydrous melting point of $MgCO_3$ at 6 GPa could be located between 1750 and 1800 °C. Under

hydrous conditions liquidus and solidus moved to lower temperatures compared to anhydrous conditions and the melting point of hydrous $MgCO_3$ at 6 GPa is located between 1700 and 1750 °C.

Introduction

One key feature in understanding the long-term carbon cycle is the knowledge of the behavior of carbon in the mantle. Therefore, outgassing of CO_2 and subduction of carbonates play an important role (Sleep & Frost 2001). Carbonates, especially $CaCO_3$ and $MgCO_3$ are the most common carbon bearing minerals on Earth and are therefore the most likely carbonates to be subducted. Findings of magnesite in high-pressure metamorphic rocks support this idea (Ogasawara et al. 2010). Experimental studies confirm the stability of e.g. magnesite, dolomite and $CaCO_3$ in different high-pressure modifications up to lower mantle conditions (Efthimiopoulos et al. 2017, Koch-Müller et al. 2016, Solopova et al. 2015, Isshiki et al. 2004, Katsura et al. 1991, Santillan & Williams 2004, Ono et al. 2005, Thomson et al. 2014).

Previous work on the anhydrous melting relations in the system $CaCO_3$ – $MgCO_3$ has been carried out at different pressures. Irving & Wyllie (1975) determined the phase diagram at 2.7 GPa, Byrnes & Wyllie (1981) at 1 GPa and more recently Buob et al. (2006) presented a phase diagram of the $CaCO_3$ – $MgCO_3$ system at 6 GPa. Problematically, Buob et al. (2006) report quenching problems in experiments within the two-phase stability fields of melt and solid. It is well known that carbonate melt is not quenchable but crystallizes very rapidly and fractionates in composition (Jones et al. 2013). This structure is referred to as spinifex structure and its bulk composition is difficult to measure by electron microprobe (EMP). Therefore, Buob et al. (2006) were not able to distinguish between melt with its spinifex structure and the solid phase in their experimental run products and could not determine experimentally the shape of

the two-phase fields. Shatskiy et al. (2014) also worked on the system $CaCO_3$ - $MgCO_3$ at 6 GPa under anhydrous conditions and made some corrections on the proposed phase diagram by Buob et al (2006), mainly with respect to the melting point of magnesite and $CaCO_3$ at 6 GPa.

The melting point of the endmember magnesite has been determined by Irving & Wyllie (1975) at 2.7 GPa and 3.3 GPa and by Katsura & Ito (1990) at 8 and 15 GPa. Recently, Solopova et al. (2015) published the melting curve of magnesite between 12 and 80 GPa from laser heated diamond anvil cell (DAC) experiments, however show relatively high errors in the temperature determination. Buob et al. (2006) and Shatskiy et al. (2014) both present melt temperatures of magnesite in the anhydrous system at 6 GPa differing by 250 °C. Buob et al. (2006) extrapolated from experiments by Irving & Wyllie (1975) and Shatskiy et al. (2014) extrapolated from experiments by Katsura & Ito (1990). Their results are plotted in Fig. 1 together with the melting curve determined by Solopova et al. (2015).

The melting point of $CaCO_3$ at 6 GPa has been determined by several studies, which fairly well agree on the melting point, located between 1600 and 1700 °C (Shatskiy et al., 2014), 1630 and 1730 °C (Suito et al., 2001) and recently it was placed at 1727 °C by Li et al. (2017). However, despite the agreement on the melting temperature it is not clear whether it is the melting point of aragonite (Shatskiy et al., 2014), or calcite V (Suito et al., 2001; Li et al., 2017).

It has been shown in an experimental study by Keppler (2003) that carbonate melt is able to dissolve a large amount of water. Keppler (2003) investigated a melt consisting of 40 wt.% of $CaCO_3$, 40 wt.% Na_2CO_3 and 20 wt.% of $MgCO_3$ and found that at a relatively low pressure of 0.225 GPa ca. 14 wt.% of water was solved in a carbonatitic melt. Such high water content must have a huge effect on the melting relations of the system. Decades ago quite a lot of experimental studies focused on the phase equilibria in the CaO-CO_2-H_2O and MgO-CO_2-H_2O systems at pressures below 1 GPa (e. g. Wyllie, 1965; Wyllie

and Tuttle, 1960). They all concluded that water could significantly reduce the melting points of carbonates. However, not much data exist for higher pressures. Shatskiy et al (2013) studied the melting behavior of the systems Na_2CO_3-$MgCO_3$ and Na_2CO_3-hydromagnesite at 6 GPa. They found in the dry system the initial melt would occur at about 1300 °C, while under hydrous conditions melt is already observed at 900 °C. Unfortunately 900 °C was the lowest temperature they studied, thus the decrease of the melt temperature may even be larger. Foustoukos and Mysen (2015) studied the structure of water-saturated carbonate melts up to 3 GPa in hydrothermal DAC's and also report a strong depression of the melting temperature in the presence of water. Thus, it is clear that there is a huge effect of the water concentration on the melting behavior at least in the above mentioned systems. To see this effect we performed a comparative study and investigated the super-solidus phase relations in the system $CaCO_3$ - $MgCO_3$ at 6 GPa under anhydrous and hydrous conditions.

Methods

For the determination of the melting point of the endmember magnesite, all experiments were conducted with either natural magnesite (< 1% impurity) for anhydrous or synthetic commercial hydromagnesite ($Mg_5(CO_3)_4(OH)_2 \cdot 4H2O$) (Alfa Aesar purity > 98 %) for hydrous conditions. The natural magnesite comes from Brumado, Brazil and the composition can be found in Tab. 1 (Helpa et al. 2014). To determine the melting relations in the $CaCO_3$-$MgCO_3$ system powdered mixtures were prepared from synthetic calcite, with 99.999 % (Aldrich; purity 99.999 %) and the natural magnesite or hydromagnesite.

Hydromagnesite, which nominally contains 23 wt.% of water, decomposes completely into water and magnesite with increasing temperature (Vágvölgyi et al. 2008). Thus, before reaching the corresponding melting temperature at high

pressure hydromagnesite will decompose into magnesite and water. As hydromagnesite contains more Mg-ions than carbonate-ions, the additional Mg-ions may be dissolved as hydrated species in the fluid phase. Using hydromagnesite allows very easily adding a controlled amount of water into the system. All materials and mixtures were dried at least at 100 °C for 24 hours. The bulk compositions for each experiment are compiled in Tab. 2. Since all samples were loaded as powders they very likely attracted an undefined amount of water from the atmosphere, which cannot be avoided unless everything is loaded in vacuum.

The experiments were conducted in a walker style multi-anvil apparatus at GFZ Potsdam. For the experiments an 18/11 assembly was used and heat was generated using a stepped graphite heater (Fig. 2). The starting material was filled into a Pt-capsule with a height of 3 mm, 2mm diameter and wall thickness of 0.2 mm. The Pt-capsules were cold sealed. Temperature was measured using Type C thermocouples, which were in contact with BN powder to prevent oxidation of the thermocouple wires. Experiments in the two-phase field of solid and melt of the Mg-rich side of the system were conducted in the rocking mode (Schmidt & Ulmer 2004). The continuous movement of ±180° with 5 °/s keeps melt and solid in movement thus achieving equilibrium. Shortly before quenching the experiments in the two-phase stability field of melt and solid, rotation was stopped allowing melt and solid to separate from each other.

During an experiment the temperature distribution within the Pt-capsule is an important issue. Walter et al. (1994) illustrated how the temperature distribution within Pt-capsule can vary depending on the experimental setup. Furthermore, they mention that a stepped heater (as used in our experiments) reduces the temperature gradient.

To prove the absence of a temperature gradient we performed two-pyroxene (enstatite - diopside) geothermometer experiments (Gasparik 1990) under similar conditions as the carbonate experiments. We took 30 to 40 EMP

146 analyses from the cross-section of each capsule (see below) of the
147 geothermometer experiments and calculate the temperatures for each analysis
148 point. From the analyses of the experiments we see that the calculated
149 temperature is close to the measured temperature and further that the
150 temperature is very homogeneously distributed (e.g. Fig. 3), e.g. thermocouple
151 reading of experiment MA407 was 1400 °C and average calculated temperature
152 was 1421 +/- 11 °C, with the variation in temperature randomly distributed over
153 the cross-section (Tab. S1).
154 In our experiments we applied the rocking mode of the press. Due to this
155 approach the extreme low-viscous carbonate melt (Kono et al., 2014) was kept
156 in movement and therefore, the temperature was homogenized within the whole
157 capsule. In experiments were melt and solid coexist we never observed
158 compositional gradients of the solid phase after quenching, which should be the
159 case if there was a noticeable temperature gradient. In many static melt
160 experiments (e.g. Shatskiy et al., 2013 and Buob et al., 2006) the melt is
161 described to occur only at the "hot part of the capsule", which was also not the
162 case in our experiments.
163
164 For the 18/11 assemblies we calibrated heating power with the measured
165 temperature. For several experiments that run with working thermocouples, the
166 heating curves were observed and then averaged. A linear fit function was
167 obtained that gives the average temperature (°C) as a function of the heating
168 power (W). In experiments where the calibration was used to determine the
169 temperature the deviation in T is +/- 50 °C, which was derived from the
170 temperature deviation of different experiments.
171 Furthermore, falling sphere experiments were conducted using the multi-anvil
172 apparatus. In the Pt-capsule of the 18/11 assembly a Pt-sphere was added to the
173 sample in the upper part of the capsule. During the preparation of the capsule
174 the sample material and the sphere where filled and stuffed into the capsule

with a hammer and a small metal rod. This may cause slight flattening of the Pt-sphere during the loading; nevertheless, the movement of the Pt-body down to the bottom of the capsule during the run indicates that the sample underwent melting. Furthermore, polishing of the capsule may as well slightly influence the shape of the Pt-body. Since Kono et al. (2014) showed by falling sphere experiments that the viscosity of carbonate melt at high pressure is ultralow, the falling sphere method is very suitable for determining at least the region of the melting temperatures.

After the runs the capsules were cut in halves, mounted in epoxy, polished and coated with carbon for EMP analyses. The falling body experiments were carefully opened at the top and the material was removed until the Pt-body was found.

The run products were analyzed using a JEOL Hyperprobe JXA-8500F EMP with a field emission cathode. As standard materials dolomite and wollastonite were used (composition found in Tab. S2). The measurement conditions varied between 10 and 15 kV acceleration voltage and 5 to 20 nA probe current. Primary grown crystals were analyzed with a focused beam with 1 μm diameter and the melt phase was measured with a defocused electron beam of 20 μm diameter on several points and averaged.

To check the reliability of the results we applied an additional method to estimate the melt composition. Measurements were done with a focused electron beam and combined with element mappings of representative areas of the melt. With the focused electron beam analyses the compositions of each mineral phase (e.g. core, rim and in between) were determined and the mappings give information on the areal distribution of the compositions. Based on the two different measurements the average composition of the quenched melt can be determined. Fig. S1 shows elemental mappings for the run MA405.

Raman measurements for phase identification were performed at GFZ Potsdam with a HORIBA Jobin Yvon LabRAM HR800 VIS spectrometer with a DPSS

laser of 473 nm wavelength. The spectral range for the measurements is 100-1200 cm^{-1} and the data acquisition time was 30s.

Samples for TEM investigations were prepared by focused ion beam (FIB) technique in a FEI FIB200TEM directly from the crystals in the microprobe mounts. Sputtering was done using Ga ions accelerated to 30 keV. The dimensions of the FIB cut were 15 x 6 x 0.15 μm^3. Details of the TEM sample preparation can be found in Wirth (2004 and 2009). These TEM foils were analyzed in a FEI Tecnai G2 F20 X-Twin Transmission electron microscope (TEM) equipped with a Schottky field emitter as an electron source. The analyses were carried out with an EDAX X-Ray analyzer in the scanning transmission mode.

Results

Melting point of magnesite at 6 GPa

Results of these experiments are shown in Tab. 3. Under anhydrous conditions the melting point of magnesite at 6 GPa could be narrowed down between 1750 and 1800 °C with the falling body method. Figure 4 shows a cross-section of an anhydrous falling body experiment at 1800 °C. The body did not completely sink to the bottom because it stuck to the wall of the capsule (not seen anymore after polishing). Furthermore, the sample clearly shows the dendritic structure of quenched melt, which beyond doubt proves the existence of melt under these conditions.

Under hydrous conditions the melting point of magnesite could be narrowed down between 1700 and 1750 °C, which is, as expected, lower than the anhydrous melting point at 6 GPa. However, the temperature in the experiment at 1750 °C was determined using the temperature calibration with the larger uncertainty.

233

234 *Determination of liquidus and solidus*

235 In the backscattered electron (BSE) images of the cross-sections of the Pt-
236 capsules from the two-phase field experiments two different phases can be
237 observed (Fig. 5). At both ends of the Pt-capsules a relatively homogeneous
238 phase with large crystals appears that is darker in the BSE image than the rest
239 of the sample. We identify this phase as the first crystallized solid in the two-
240 phase field. The rest of the capsule is filled with a second phase, which is the
241 quenched melt. By Raman spectroscopic measurements we identified both
242 phases at the Pt-capsules end and the elongated small crystals from the
243 quenched melt as Mg-Ca-carbonates.

244 To verify that the observed separation of melt and solid is an effect caused by
245 the experimental procedure of first stopping the rotation and then quenching the
246 experiment and not by a temperature gradient, we quenched an experiment and
247 did not stop the rotation the press. By that, the solid magnesite could not
248 separate itself from the melt phase, as it would have when the rotation stopped.
249 Thus, we found many small magnesite grains caught within the quenched melt
250 phase that is present all over the capsule (Fig. 6 A-C). We therefore conclude
251 that the stop of the rotation before the quenching is essential to the separation of
252 melt and solid in our experiments.

253 At the Mg-rich side of the phase diagram under anhydrous as well as under
254 hydrous conditions we found that the quenched melt consists of several
255 elongated very small crystals. These are randomly distributed and show in the
256 BSE images the fractionation mentioned above, i.e., zoning from dark contrast
257 in the middle of the crystal (Mg-rich) to bright contrast at the rim (Ca-rich).

258 Under anhydrous conditions at the Ca-rich side of the phase diagram, the
259 quenched melt as well consists of several elongated very small crystals.
260 However, they are not visibly fractionated as the crystals of the Mg-rich side of
261 the phase diagram.

Under hydrous conditions the quenched melt additionally contains brucite, as identified by Raman spectroscopy, which most probably formed during quenching. As hydromagnesite contains more magnesium than carbon, the quenched brucite crystals most likely form due to the extra magnesium and the water.

The hydrous experiment in the subsolidus region at 1200°C shows dolomite and magnesite (Fig. 7) but both compositions deviate strongly from the anhydrous results of Buob et al. (2006), which needs further investigation. Nevertheless, this proves that hydromagnesite and calcite react and decompose into carbonates and water at high pressure and temperature. Additionally, a lot of porosity can be observed, which is explicable by the high amount of water within the system.

The results of the EMP analyses are shown in Tab. 2. At one temperature the composition of coexisting melt and crystal defines the shape of the two-phase field and thus the position of the liquidus and solidus. Some experiments were performed at superliquidus and some at subsolidus conditions.

To prove the benefit of using the rotating multi-anvil press one has to compare our data with the raw data from Buob (2003), which she obtained in quenched static multi-anvil runs for her PhD thesis (their Fig. 5-2). The first melt for the Mg-rich part of the system occurs at 1350 °C and was studied until 1600 °C. However, the scatter of the data in the Mg-rich part of the system (seven experiments) does not allow any precise interpretation of the solid-liquid relations (Buob, 2003). Consequently, the phase diagram presented in Buob et al. (2006) for the Mg-rich part is only an estimate based on two of these experiments.

Fig. 8 shows our results as T-x phase diagrams for 6 GPa in comparison to the proposed phase diagram by Buob et al. (2006). Due to our new approach of using a rotating multi-anvil apparatus we clearly could overcome the quenching problems reported in previous studies.

Buob et al. (2006) conclude that at 5.3 GPa and 900 °C Ca-Mg disorder in dolomite begins. Therefore, carbonates of dolomitic composition are referred to as disordered carbonate phases. Under anhydrous conditions (Fig. 8a) we determined the liquidus of the stability field of magnesite + melt at 50 to 100 °C higher temperatures than suggested by Buob et al. (2006). This is in line with the higher melting point of the endmember magnesite at 6 GPa as determined in this study. The peritectic line is found at 1300 °C, which is ca. 50 °C lower than previously estimated by Buob et al. (2006). The peritectic point is at a composition of X_{Mg}= 0.37, as determined from the Ca-rich melt phase (white phase Fig. 9). The composition of the Ca-bearing magnesite (X_{Mg}= 0.85) (dark grey in Fig. 9), which is close to the composition of the peritectic line of Buob et al. (2006), and the disordered carbonate phase (X_{Mg}= 0.58) (medium grey in Fig. 9) delimit the width of the miscibility gap of Ca-bearing magnesite and the disordered carbonate phase at this temperature.

At the Mg-rich side the solidus is almost the same as the one from Buob et al. (2006) with the difference of now being extended to higher temperatures. Especially, the liquidus is shifted now to more Ca-rich composition than suggested by Buob et al (2006), which may reflect their difficulties measuring the melt composition. Liquidus and solidus of the field of $CaCO_3$ + melt were found to be at 50 to 100 °C lower temperature than Buob et al. (2006) suggested. The minimum melt point at 6 GPa suggested by us moved from a mole fraction of X_{Mg}= 0.51 at 1350 °C (Buob et al., 2006) to X_{Mg}= 0.3 - 0.35 at temperatures below 1300 °C.

Thus, compared to the phase diagram published by Irving and Wyllie (1975) for 2.7 GPa (corrected value from Byrnes and Wyllie, 1981) pressure has a strong effect on the melting behavior.

Our hydrous results show that liquidus and solidus of the stability field of magnesite + melt moved to lower temperatures compared to the anhydrous

system, as expected (Fig. 8b). A direct comparison with anhydrous and hydrous results overlapping can be found in Fig. 8c.

Raman spectroscopy

We measured Raman spectra of both anhydrous and hydrous experiments in the OH-stretching region and could find bands corresponding to the OH-stretching of portlandite and brucite located at ca. 3600 and 3650 cm^{-1} (Fig. 10) (Lutz et al. 1994; Duffy et al. 1995). Brucite was only found in regions of former melt, thus implying that all water was dissolved in the melt. Even though the solid phase under hydrous conditions seems to show the brucite peak at 3650 cm^{-1} this as well might come from the melt. Due to the spatial resolution of the Raman setup we most likely have measured melt inclusions in the solid. In addition, small portions of melt are sometimes found at the grain boundaries of the solid phases.

Even under nominally anhydrous conditions we found the brucite peak at 3650 cm^{-1} in the spectra of the melt. During the sample preparation $MgCO_3$ powder attracts water, leading to small amounts of water in the experiment. From the Raman spectra of experiment MA451 we observe broadening of the Raman active modes. This might be an effect of disordering, since the melt phase is quenched to a disordered carbonate (Buob et al. 2006).

Samples MA513 and MA515 from experiments at the Ca-rich side both were completely molten at temperatures of 1575 °C and 1620 °C and afterwards quenched. Raman measurements of the run products of both experiments show peak positions (Fig. 11) that are very close to the results of Rutt & Nicola (1974) for calcite.

Occurrence of Pokrovskite under hydrous conditions

Under hydrous conditions in the experiments above 1470 °C the overall appearance changes (MA423, MA428 and MA452). In the cross-section

through the capsule we did not observe a separation of melt and solid but fractionated melt with large elongated crystals (Fig. 12).

XRD and Raman spectroscopic measurements of sample MA423 verified that the elongated phase is pokrovskite with the stoichiometry $Mg_2(CO_3)(OH)_2$*0.5 H_2O. From Rietveld refinement we obtained the lattice parameters a = 12.33 Å, b = 9.30 Å, c =3.13 Å and β = 95.85°, which are in fairly good agreement with the lattice parameters given by Perchiazzi and Merlino (2006) a = 12.2396(4) Å, b = 9.3506(4) Å, c = 3.1578(1) Å, β = 96.445(5)°. The mineral phase is very unstable under the electron beam and therefore the EMP analyses of this mineral are very inconsistent. This behavior can be explained by high water concentration in the mineral investigated. Electron diffraction pattern of that mineral also confirm pokrovskite. The electron diffraction pattern was indexed comparing the observed d-spacing and angles between adjacent planes based on the structural data by Perchiazzi and Merlino (2006). Fig. 13 shows the electron diffraction pattern and Tab. 4 the d-spacing and angles between the diffraction spots and the calculated data. The observed data match approximately the calculated data. For the angles the deviation between the measured and observed is less than 2° and for the d-spacing the largest observed deviation between the calculated and observed data is 0.25 Å in the (140) plane. The deviation between observed and calculated data can be explained by dehydration of the phase during electron irradiation. In the bright-field image (Fig. 13A) of the sample alternating bright and dark thin contrasted lamellae from left to right can be observed. These contrasts resemble exsolution features observed in feldspar (spinodal decomposition). In the electron diffraction image (Fig. 13B) the presence of very thin lamellae is documented by streaks along in [100] direction.

Discussion

We determined the stability fields of melt and solid of the $CaCO_3$-$MgCO_3$ phase diagram at 6 GPa and up to 1800 °C under anhydrous conditions. Additionally, we performed hydrous experiments at in the stability field of melt and solid at the Mg-rich side of the phase diagram. With the help of the rotating multi-anvil experiments the reported quenching problems could be overcome. With the experimental setup melt and first crystallized solids could easily be separated and afterwards analyzed. Furthermore, the results of this study show the importance of achieving equilibrium when dealing with phase relations in super-solidus experiments since our results of the anhydrous experiments strongly deviate from the results of Buob et al. (2006). Overall, it can be stated that in high pressure and temperature melting experiments rotation of the press clearly supports homogenizing of the melt and thus achieving equilibrium.

Melting of the magnesite and calcite endmember at 6 GPa

We were able to determine the melting point of magnesite at 6 GPa. Under anhydrous conditions the melting point is found in the range of 1750 and 1800 °C. This is higher than the estimate of 1650 °C of Buob et al. (2006) and lower that the estimate of 1900 °C of Shatskiy et al. (2014). On the Ca-rich side of the phase diagram it is not clear whether at 6 GPa the $CaCO_3$ endmember melts in the calcite-V structure (Li et al., 2017) or in the aragonite structure (Shatskiy et al., 2014). The quenched run products of our close to Ca-endmember experiments show calcite structure, thus favoring the stability of calcite-V under these conditions.

Under hydrous conditions the melting point is between 1700 and 1750 °C. This is still higher than the extrapolation from Buob et al. (2006) (1650 °C). But, as to be expected lower as the melting point anhydrous conditions in this study.

It is a commonly known fact that water can reduce the melting point of a solid phase severely. Thus, it is surprising that the melting point of $MgCO_3$ is only 50

406 – 100 °C lower under hydrous conditions compared to the anhydrous
407 conditions. Nevertheless, a lowering of 50 - 100 °C is, within error, the same as
408 the lowering of the solidus under hydrous conditions.
409 Furthermore, melting can be accelerated by displacements within the crystal
410 structure that form due to the incorporation of water into the crystal structure.
411 To the best of our knowledge magnesite does not belong to the group of
412 nominally anhydrous minerals. By Raman spectroscopy we do not see any
413 evidence that water is incorporated into the structure and most likely exclude
414 this effect. Wyllie and Tuttle (1960) studied the system $CaCO_3$ and water at 0.1
415 GPa. They see, in difference to our results, a lowering of the melting point from
416 1300 °C to 1000 °C with 20 wt.% of water. Possible reasons for this different
417 behavior might be the much higher pressure applied in our study and/or a
418 different behavior of $CaCO_3$ under the presence of water compared to $MgCO_3$.
419
420 *Determination of liquidus and solidus at 6 GPa*
421 Under hydrous conditions the additional Mg, which comes from the
422 decomposition of hydromagnesite into magnesite, Mg-ions and water, is under
423 subsolidus conditions dissolved as hydrated species within the fluid or at higher
424 temperatures within the melt. During quenching it is precipitated as brucite and
425 this may lead to slightly too Mg-rich analyses of the quenched melt due to
426 mixed EMP analyses. Thus, it may be that the hydrous liquidus in Fig. 8b
427 should be slightly shifted to more Ca-rich compositions.
428 As a consequence, the lever rule cannot be applied to quantify the amount of
429 solid and melt phase and it is also not possible to quantify the amount of water.
430 But, in all hydrous experiments the amount of solid phase was relatively low.
431 Due to the fact that probably all water went into the melt phase and due to the
432 low amount of the solid phase, we can state that the amount of water in the melt
433 phase is ca. 18 to 20 wt.% (Tab. 3).

Under anhydrous conditions the liquidus and solidus of the stability field of magnesite + melt both moved about 50 to 100 °C to higher temperatures, with respect to the results from Buob et al. (2006). Water strongly fractionates into the melt phase (and is absent in the solids) and does decrease the two phase stability field of melt and solid about 100 to 200 °C towards lower temperature and more Mg-rich compositions. Under anhydrous conditions liquidus and solidus of the Ca-rich side of the phase diagram moved about 50 to 100 °C to lower temperatures, with respect to the results of Buob et al. (2006).

Most of the results of the anhydrous and hydrous liquidus are based on defocused electron beam measurements. But for samples MA403 and MA 405 the compositions were also determined with a combination of elemental mappings and spot analyses as described above and shown in Fig. S1. The results are shown in Tab. 5. Both methods yield similar results. We proved herewith the reliability of the defocused beam measurements.

Separation of melt and solid

The separation of melt and solid during the experiment and the applied run conditions, which have produced a large amount of melt, facilitated the analyses of the run products substantially. The previously reported quenching problems were not encountered, even though the melt phase strongly fractionated. In all experiments that run in the two-phase field of melt and solid, regardless of the water content, it could be demonstrated that at the bottom and at the top of the capsule was a solid phase. This observation is contrary to the primary idea that when the rotation is stopped all the solid phase, which is floating through the melt, should sink to the bottom of the capsule. We think that we are in equilibrium during the rotations, but at such high temperature of more than 1300 °C and with the ± 180 ° rotations parts of the solid phase stick at each end of the capsule and serves as a nucleation site.

Another potential explanation for the observation of the solid phase at the top and bottom of the capsule is a temperature gradient within the capsule, which is a common issue in multi anvil experiments (e.g. Rubie, 1998). However, we most likely exclude this issue, because of our experimental setup.

The occurrence of pokrovskite under hydrous conditions

Pokrovskite occurs during quenching. This is obvious from the crystal shapes that clearly resemble rapidly cooled quench crystals. If pokrovskite was not a quench phase it would imply that above ca. 1500 °C a new stability field of pokrovskite and melt would appear and on the Mg-rich side of the phase diagram at temperatures between 1500 °C and the melting point 100 % pokrovskite should be stable. Experiments MA465 and MA468 run at 1500 °C and 1550 °C right in the area were 100 % pokrovskite should be stable but clearly show no areas of quenched melt but instead solid magnesite.

Implications

As solid carbonates do not seem to incorporate water, subduction of carbonates, in difference to silicates, probably does not play a role in the deep water cycle. On the other side, as shown by Keppler (2003) and in our study, carbonate melt is able to incorporate a large amount of water. In the upper mantle at 6 GPa we would expect a temperature of ca. 1200 – 1600 °C (depending on the geothermal gradient) and since we see the first melting at ca. 1400 °C under hydrous conditions such high amounts of water would clearly induce carbonate melting. However, we needed about 20 wt.% of water to lower liquidus and solidus about 100 – 200 °C, an amount unrealistically high in the deep Earth. Nevertheless, more experiments are needed to fully understand hydrous carbonate melting under pressure.

Acknowledgements

We thank Andreas Ebert and Reiner Schulz for the technical support during the experiments and Vanessa Helpa for providing the magnesite sample. This work is partly supported by the DFG funded research group FOR2125 CarboPaT (KO1260/16).

References cited

Buob, A. (2003) The system $CaCO_3$-$MgCO_3$: Experiments and Thermodynamic Modeling of the Trigonal and Orthorhombic Solid Solutions at High Pressure and Temperature, 172 p. Ph.D. thesis, Swiss Federal Institute of Technology, Zurich.

Buob, A., Luth, R., Schmidt, M. & Ulmer, P. (2006) Experiments on $CaCO_3$-$MgCO_3$ solid solution at high pressure and temperature, American Mineralogist 91, 435-440.

Byrnes, A. & Wyllie, P. (1981) Subsolidus and melting relations for the join $CaCO_3$-$MgCO_3$, Geochimica et Chosmochimica Acta 45, 321-328.

517 Duffy, T.S., Meade, C., Fei, Y., Mao, H.-K. and Hemley, R.J. (1995), High
518 pressure phase transition in brucite, $Mg(OH)_2$, American Mineralogist 80, 222-
519 230.

520 Efthimiopoulos, I., Jahn, S., Kuras, A., Schade, U., Koch-Müller, M. (2017)
521 Combined high-pressure and high-temperature vibrational studies of dolomite:
522 phase diagram and evidence of a new distorted modification, Phys. Chem.
523 Minerals, doi:10.1007/s00269-017-0874-5.

524 Foustoukos D.I. and Mysen B.O. (2014) The structure of water-saturated
525 carbonate melts, American Mineralogist 100, 35-46.
526
527 Gasparik, T. (1990), A thermodynamic model for the enstatite-diopside join,
528 American Mineralogist 75, 1080-1091.
529
530 Helpa, V., Rybacki, E., Abart, R., Morales, L., Rhede, D., Jebek, P. & Dresen,
531 G. (2014, Reaction kinetics of dolomite rim growth, Contributions to
532 Mineralogy and Petrology 167.
533
534 Irving, A. & Wyllie, P. (1975) Subsolidus and melting relationships for calcite,
535 magnesite and the join $CaCO_3$-$MgCO_3$ to 36 kb, Geochimica et Cosmochimica
536 Acta 39, 35-53.
537
538 Isshiki, M., Irifune, T., Hirose, K., Ono, S., Ohishi, Y., Watanuki, T., Nishibori,
539 E., Takata, M. & Sakata, M. (2004) Stability of magnesite and its high-pressure
540 form in the lowermost mantle, Nature 427, 60-63.
541
542 Jones, A., Genge, M. & Carmody, L. (2013) Carbonate melts and carbonatites,
543 Reviews in Mineralogy and Geochemistry 75, 289-322.

Katsura, T. & Ito, E. (1990) Melting and subsolidus phase relations in the $MgSiO_3$-$MgCO_3$ system at high pressures: implications to evolution of the Earth's atmosphere, Earth and Planetary Science Letters 99(12), 110-117.

Katsura, T., Tsuchida, Y., Ito, E., Yagi, T., Utsumi, W. & Akimoto, S. (1991) Stability of magnesite under lower mantle conditions, Proceeding of the Japan Academy B 67, 57-60.

Koch-Müller, M., Jahn, S., Birkholz, N., Ritter, E., Schade, U. (2016) Phase transitions in the system $CaCO_3$ at high P and T determined by in situ vibrational spectroscopy in diamond anvil cells and first-principles simulations, Phys. Chem. Minerals, 43, 545-561.

Kono, Y, Kenney-Benson, C., Hummer, D., Ohfuji, H., Park, C., Shen, G., Wang, Y., Kavner, A. & Manning, C.E. (2014) Ultralow viscosity of carbonate melts at high pressures. Nature Communication. 5:5091.

Li, Z., Li, J., Lange, R., Liu, J., Militzer, B. (2017) Determination of calcium carbonate and sodium carbonate melting curves up to Earth's transition zone pressures with implications for the deep carbon cycle, Earth and Planetary Science Letters 457, 395-402.

Lutz, H.D., Möller, H. & Schmidt, M. (1994) Lattice vibration spectra. Part LXXXII. Brucite-type hydroxides $M(OH)_2$ (M=Ca, Mn, Co, Fe, Cd) – IR and Raman spectra, neutron diffraction of $Fe(OH)_2$, Journal of Molecular Structure 328, 121-132.

Ogasawara, Y., Ohta, M., Fukasawa, I. & Maruyama, S. (2000) Diamond bearing and diamond free metacarbonate rocks from Komdy-Kol in the Kokchetav massif, northern Kazakhstan, The Island Arc 9, 400-416.

Ono, S., Kikegawa, T., Ohishi, Y. & Tsuchiya, J. (2005) Post-aragonite phase transformation in $CaCO_3$ at 40 GPa, American Mineralogist 90, 667-671.

Perchiazzi, N. and Merlino, N. (2006) The malachite-rosasite group: crystal structures of glaukosphaerite and pokrovskite, European Journal of Mineralogy 18, 787-792.

Rutt, H.N. & Nicola, J.H. (1974): Raman spectra of carbonates of calcite structure, J. Phys. C. Solid State, **7**, 4522-4528.

Santillan, J. & Williams, Q. (2004) A high pressure x-ray diffraction study of aragonite and the post-aragonite phase transition in $CaCO_3$, American Mineralogist 89, 1348-1352.

Schmidt, M. & Ulmer, P. (2004) A rocking multianvil: elimination of chemical segregation in fluid-saturated high-pressure experiments, Geochimica et Cosmochimica Acta 68(8), 1889-1899.

Shatskiy, A., Bordzov, Y., Litasov, K., Kupriyanov, I., Ohtani, E. & Palyanov, Y. (2014) Phase relations in the system $FeCO_3$-$CaCO_3$ at 6 GPa and 900-1700 °C and its relations to the system $CaCO_3$-$FeCO_3$-$MgCO_3$, American Mineralogist 99, 773-785.

Sleep, N. & Frost, D. (2001) Carbon dioxide cycling and implications for climate on ancient Earth, Journal of Geophysical Research 106, 1373-1399.

Solopova, N.A., Dubrovinsky, L., Spival, A.V., Litivin, Y.A. & Dubrovinskaia, N. (2015) Melting and decomposition of $MgCO_3$ at pressures up to 84 GPa, Physics and Chemistry of Minerals 42, 73-81.

Suito, K., Namba, J., Horikawa, T., Taniguchi, Y., Sakurai, N., Kobayashi, M., Onodera, A., Shimomura, O. & Kikegawa, T. (2001) Phase relations of $CaCO_3$ at high pressure and high temperature, American Mineralogist 86, 997-1002.

Thomson, A.R, Walter, M.J., Kohn, S.C. & Lord, O.T. (2014) Experimental determination of melting in the systems Enstatite-Magnesite and Magnesite-Calcite from 15 to 80 GPa, American Mineralogist 99, 1544-1554.

Vágvölgyi, V., Frost, R., Hales, M., Locke, A., Kristof, J. & Neuville, D. (2008) Controlled rate thermal analysis of hydromagnesite, Journal of Thermal Analysis and Calorimetry 92(3), 893-897.

Wirth, R. (2004) A novel technology for advanced application of micro- and nanoanalysis in geosciences and applied mineralogy. European Journal of Mineralogy, 16:863–876.

Wirth, R. (2009) Focused ion beam (FIB) combined with SEM and TEM: Advanced analytical tools for studies of chemical composition, microstructure and crystal structure in geomaterials on a nanometre scale. Chemical Geology, 261:217–229.

Wyllie, P.J. and Tuttle, O.F. (1960) The System $CaO-CO_2-H_2O$ and the Origin of Carbonatites, Journal of Petrology, 1:1-46.

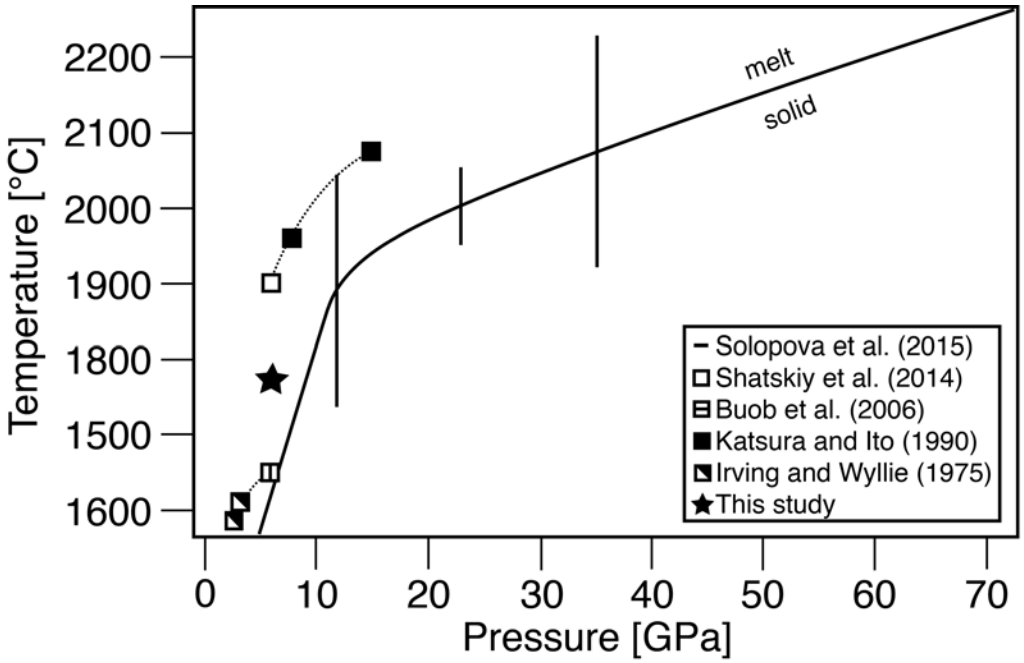

Fig. 1 Melting temperature of magnesite as a function of pressure. The solid/melt line correspond to the results of Solopova et al. (2015) and the vertical lines indicate the uncertainties in temperature in their DAC runs (+/- 150 °C) and in their multi-anvil run at 23 GPa (+/- 50 °C). The data labeled Irving and Wyllie (1975) and Katsura and Ito (1990) are experimentally determined; the points labeled Buob et al. (2006) and Shatskiy et al. (2014) are extrapolations.

This is a preprint, the final version is subject to change, of the American Mineralogist (MSA)
Cite as Authors (Year) Title. American Mineralogist, in press.
(DOI will not work until issue is live.) DOI: http://dx.doi.org/10.2138/am-2017-5831

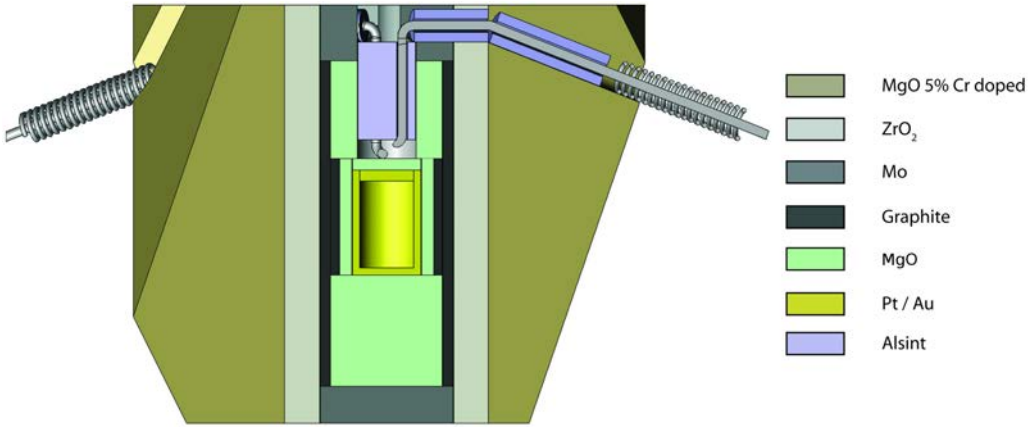

Fig. 2 Cross-section of the MgO octahedron (brown) used for our experiments. In yellow is the sample capsule, black the stepped graphite heater. The grey thermocouple is measuring the temperature at the upper side of the Pt-capsule and secured from breaking by Alsint tubing and wires made out of the thermocouple material. Both, the capsule and the thermocouple are fixed in MgO tubings (light green). In dark grey are molybdenum plates, which ensure electrical contact of the outer circuit with the heater.

Fig. 3 Cross-section of an exemplary two-pyroxene geothermometer experiment. The red numbers give the calculated temperatures and show, over all, a very homogeneous temperature distribution within the Pt-capsule.

This is a preprint, the final version is subject to change, of the American Mineralogist (MSA)
Cite as Authors (Year) Title. American Mineralogist, in press.
(DOI will not work until issue is live.) DOI: http://dx.doi.org/10.2138/am-2017-5831

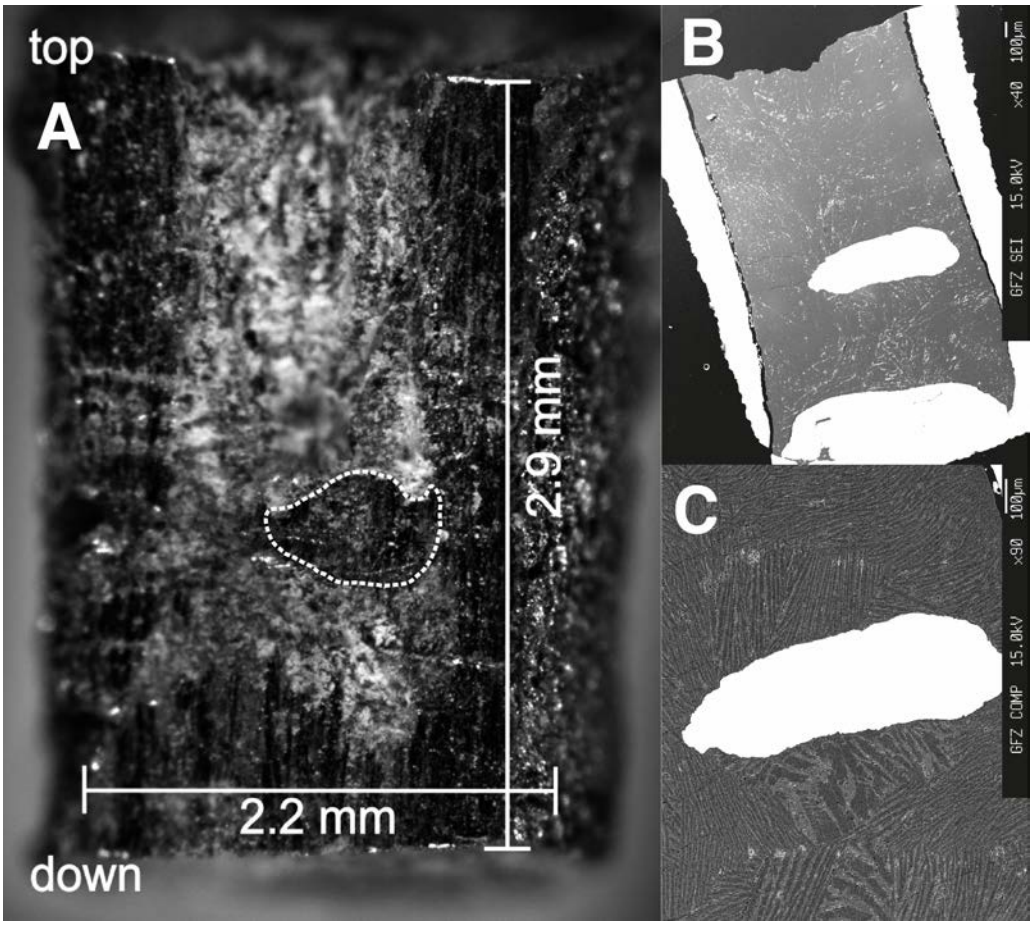

Fig. 4 Cross-section of a capsule of an anhydrous falling body experiment at 1800 °C. A: The Pt-body did not completely fall to the bottom of the capsule because it stuck to the capsules wall. B: Due to polishing after taking photo A the contact of the Pt-sphere/body with the capsule is not visible anymore, which leaves one under the impression that the Pt-sphere/body did not sink. C: In the magnification around Pt-sphere/body dendritic melt structure is clearly visible, which prove melting without any doubt.

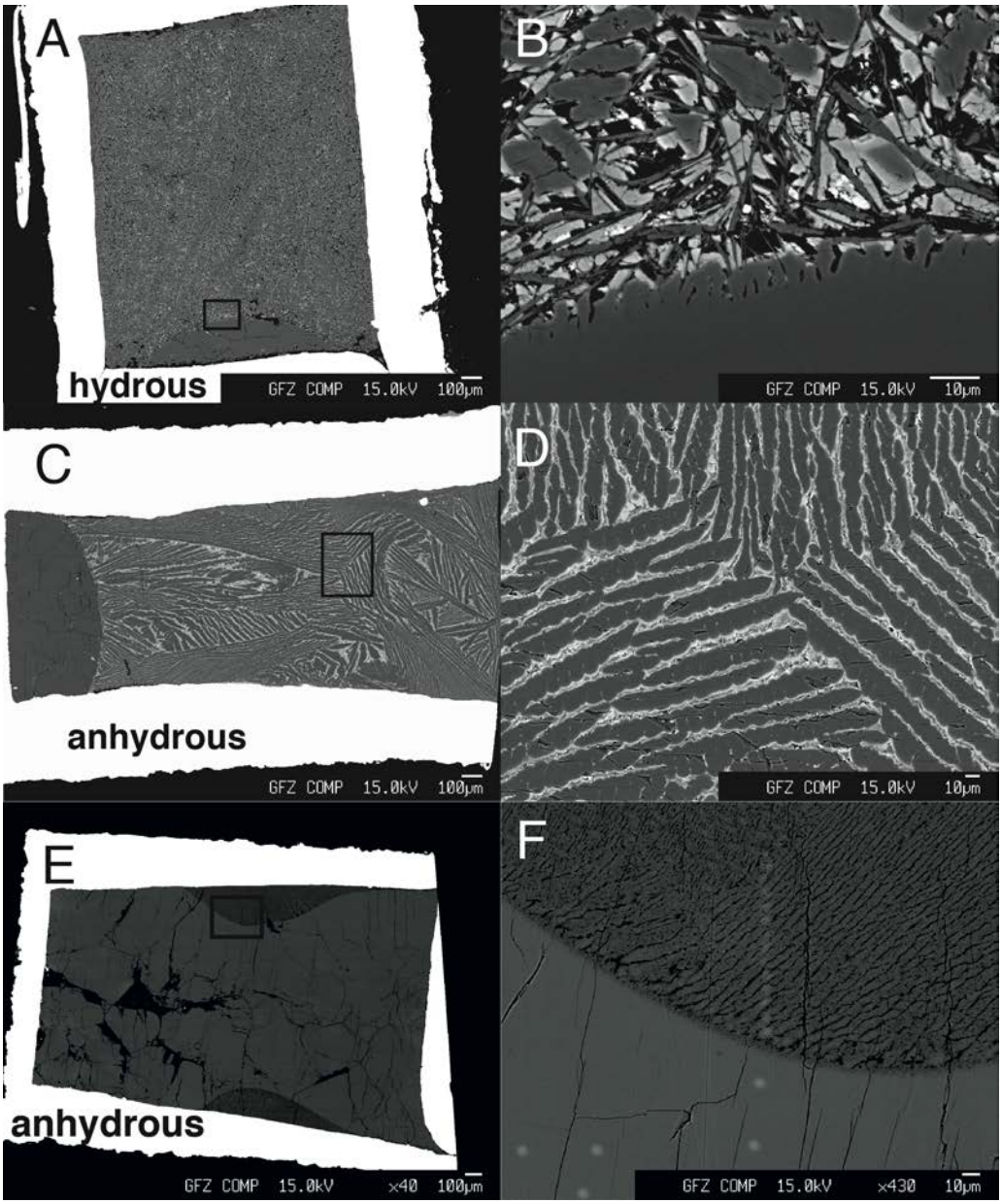

675

676 Fig. 5 A, C, E: BSE pictures of cross-sections of the recovered capsules of the
677 hydrous experiment MA403 (A), of the anhydrous experiment MA449 (C) and
678 the anhydrous experiment MA517 (E). White colors represent the Pt-capsules.
679 A: The experiment has been performed at the Mg-rich side of the phase
680 diagram. At the top and at the bottom of the capsule the slightly darker primary
681 grown magnesite is found and in between the melt phase. B: Close up look at

682 the melt and the solid phase (dark grey at the bottom) of (A). The melt phase is
683 fractionated into brighter more calcium rich magnesite, a darker calcium poor
684 magnesite, dark brucite needles and porosity, as indicated by black color. C:
685 The experiment has been performed at the Mg-rich side of the phase diagram.
686 At the bottom of the capsule of the anhydrous experiment MA449 the slightly
687 darker solid magnesite is found and the rest is strongly fractionated melt phase
688 D: Close up look at the melt of (C). The melt fractionated into elongated
689 crystals that are Mg-rich in the center and have more Ca-rich rims. E: The
690 experiment has been performed at the Ca-rich side of the phase diagram. At
691 both sides of the capsule darker half round areas of melt are found. During the
692 sample preparation larger pieces went lost, thus, the black areas. F: Close up
693 look at the melt and solid phase of (E). The melt is Ca-rich and did not visibly
694 fractionate into different compositions as in (C). The brighter dots come from
695 the EMP analyses.

696

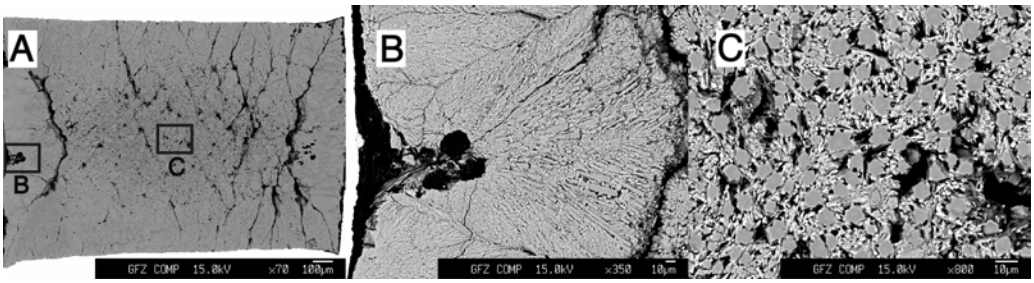

697

698 Fig. 6 A) Cross-section of a hydrous rotating experiment at 1350 °C. The
699 experiment was quenched during the rotation. In difference to the previous
700 experiments melt and solid could not be separated. B) Detailed view of the
701 bottom of the capsule. Spinifex structure clearly indicates the former presence
702 of melt in an area were we usually would have expected solid magnesite. C)
703 Detailed view of the center of the capsule. Magnesite grains are found within

the melt phase and could not fall to the bottom of the capsule because of the rotation.

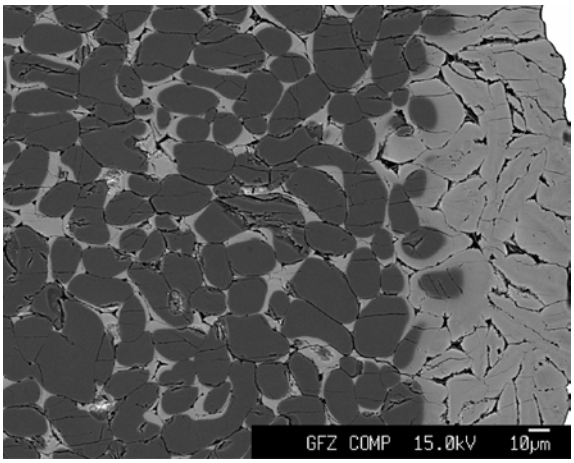

Fig. 7 Hydrous experiment run at 1200 °C in the stability field of disordered carbonate (light grey) and magnesite (dark grey). During the experiment water went into the pore space, as indicated by frequently found brucite needles.

This is a preprint, the final version is subject to change, of the American Mineralogist (MSA)
Cite as Authors (Year) Title. American Mineralogist, in press.
(DOI will not work until issue is live.) DOI: http://dx.doi.org/10.2138/am-2017-5831

720

721

722

723

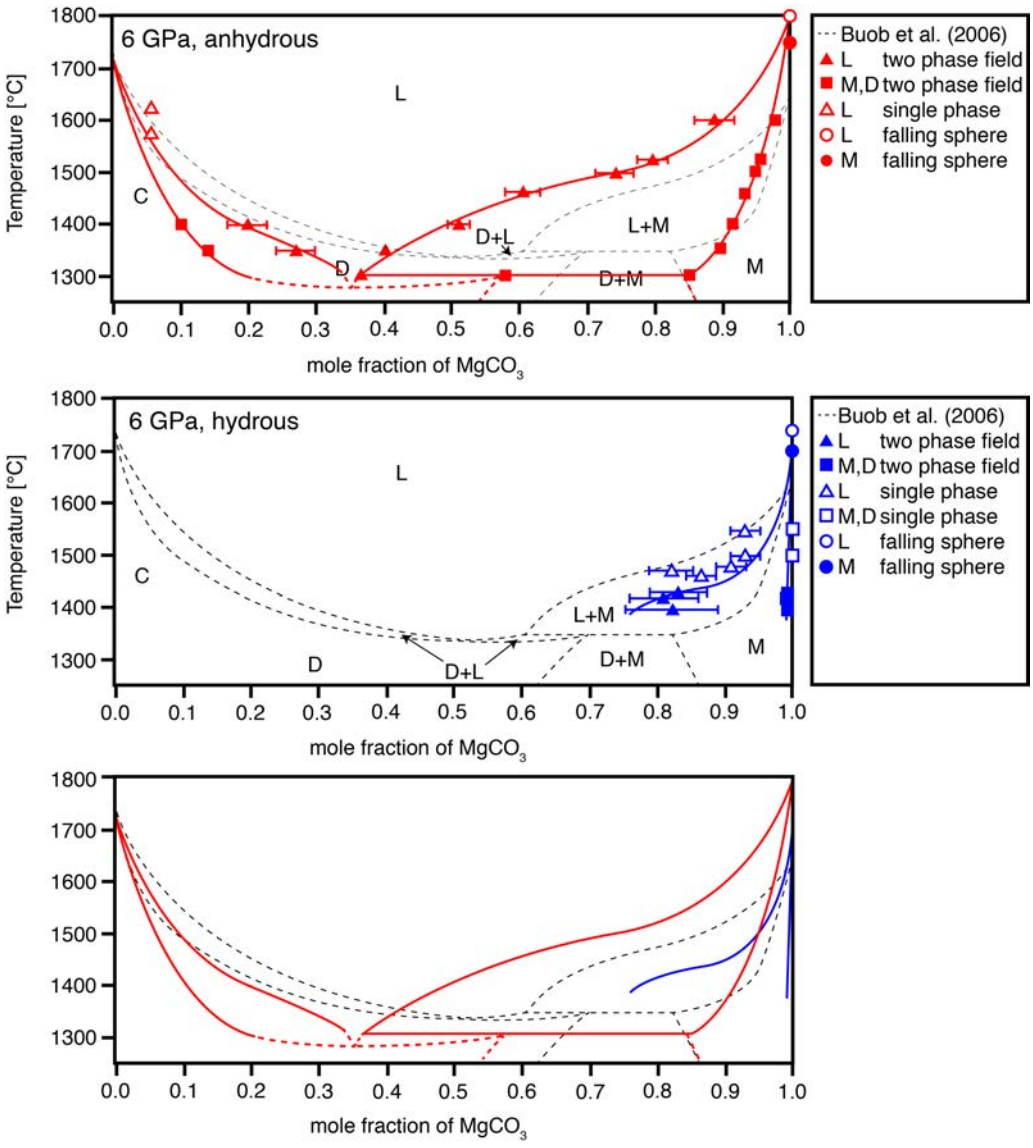

724

Fig. 8 A: Stability field of melt and solid under anhydrous conditions. The dotted lines are the results from Buob et al. (2006) and the solid red lines from this study. B: Phase diagram under hydrous conditions. The dotted lines are the results from Buob et al. (2006) and the solid blue lines from this study. C: Direct comparison of the anhydrous results with the preliminary hydrous results. M stands for magnesite, D for disordered carbonate (Buob et al., 2006) and L for liquid. The labeling posititions in the phase diagram are based on Buob et al. (2006). Closed symbols indicate coexistence of solid and melt; open symbols were performed in the super-liquidus field or in the subsolidus field of magnesite. Experiments resulting in pokrovskite plus melt are plotted in the super-liquidus field with the bulk composition of the starting material. The temperature uncertainty for the experiments is +/- 50 °C.

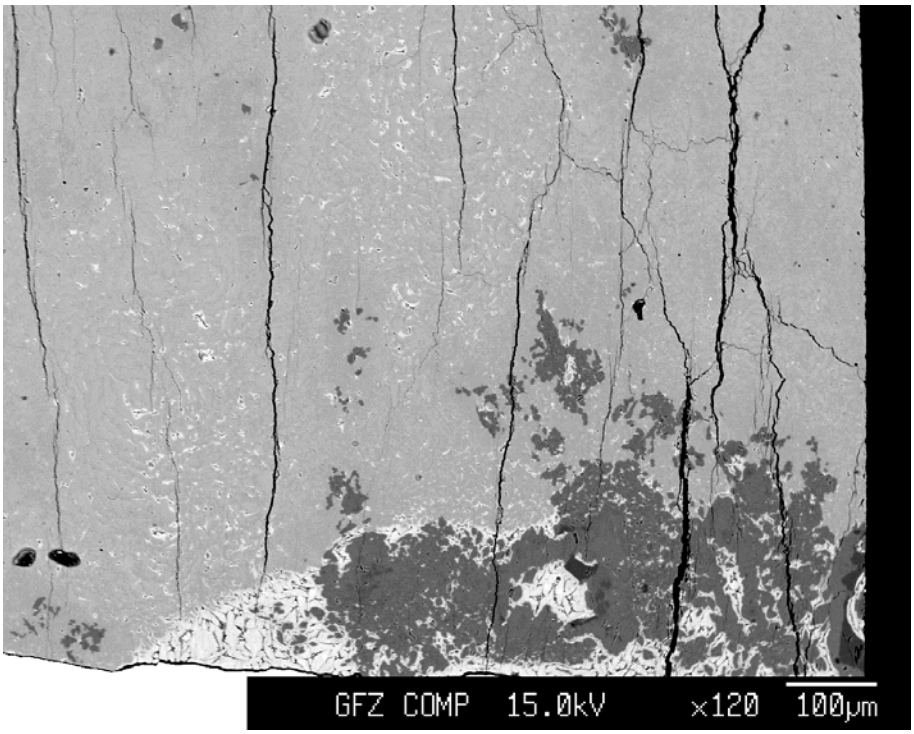

Fig. 9 Detailed view of experiment MA511. The white color represents a Ca-rich melt phase, light grey a dolomite and dark grey Ca-bearing magnesite. This experiment run at 1300 °C and exhibits the first occurrence of melt of the Mg-rich side of the phase diagram.

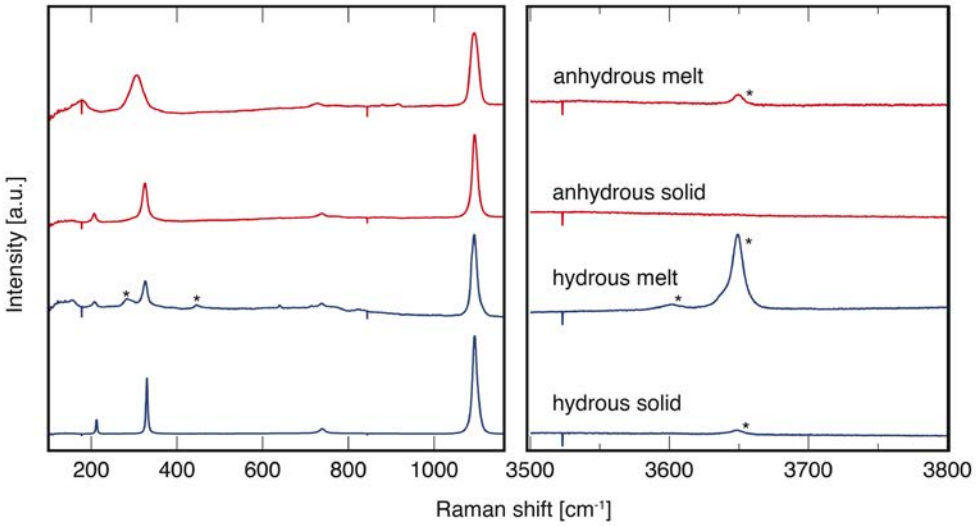

Fig. 10 Raman spectra of a hydrous and an anhydrous experiment. Marked with an asterix are the peaks belonging to $Mg(OH)_2$ or $Ca(OH)_2$ (Lutz et al. 1994). Even in the nominally anhydrous experiment brucite is found, which indicates that the starting material attracted atmospheric water. In the anhydrous experiment the broadening of the peaks in the melt phase is typical for disordered carbonate.

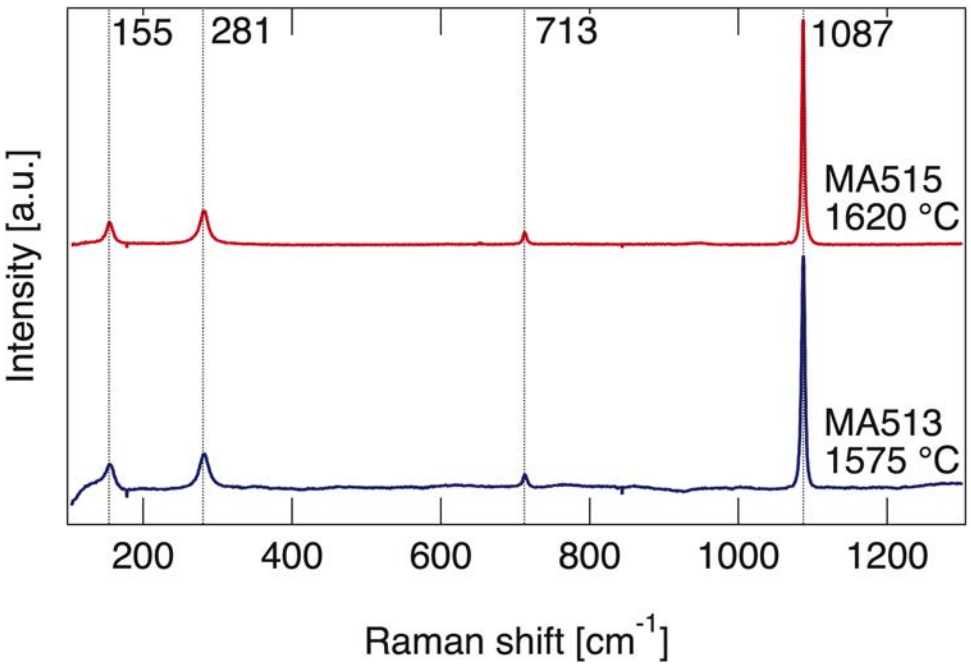

Fig. 11 Raman spectra of samples MA513 and MA515. Both experiments were run in the stability field of melt and were quenched to calcite. The Raman peak positions are very similar to the ones reported by Rutt & Nicola (1974).

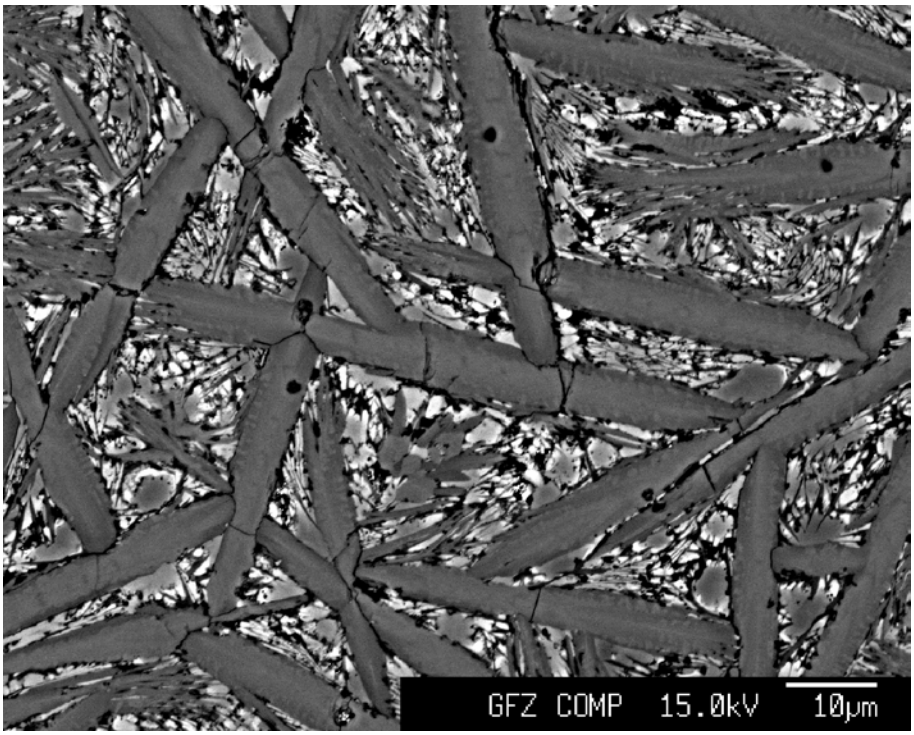

Fig. 12 Cross-section of sample MA452. The elongated crystals are pokrovskite, which formed during quenching. The small fractionated crystals are interpreted as quenched melt. The experimental run conditions are interpreted to be in the superliquidus field.

This is a preprint, the final version is subject to change, of the American Mineralogist (MSA)
Cite as Authors (Year) Title. American Mineralogist, in press.
(DOI will not work until issue is live.) DOI: http://dx.doi.org/10.2138/am-2017-5831

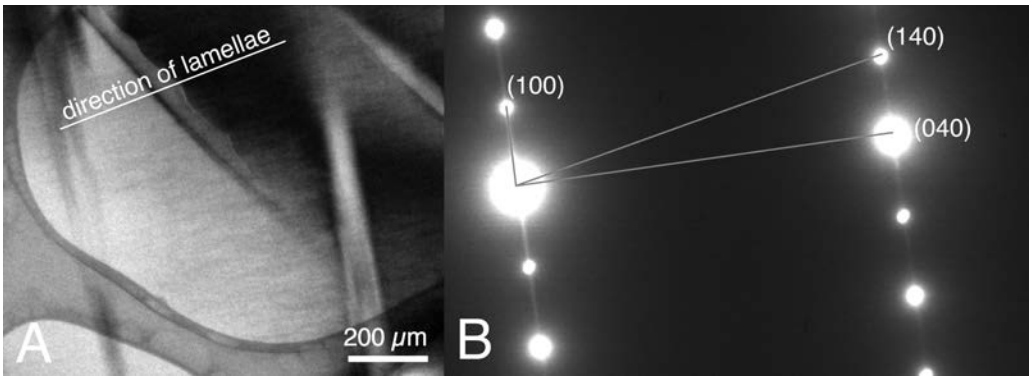

Fig. 13 A: Bright field image of the FIB cut of sample MA423 showing light streaks from left to right. It is not clarified what causes the streaks from top to bottom. On the left and on the bottom of the image the copper grid is found. B: Electron diffraction image of sample MA423 showing the (100)-, (140)- and (040)-lattice plane. The angle between 100 and 140 is 77.5° and between 040 and 140 is 12°.

This is a preprint, the final version is subject to change, of the American Mineralogist (MSA)
Cite as Authors (Year) Title. American Mineralogist, in press.
(DOI will not work until issue is live.) DOI: http://dx.doi.org/10.2138/am-2017-5831

803 Tab.1 Composition of the magnesite used in this study (Helpa et al., 2014).

	wt.%
MgO	46.08±1.65
FeO	0.18±0.05
CaO	0.26±0.04
SrO	0.02±0.01
MnO	0.04±0.03
TiO_2	0.01±0.01
SiO_2	0.01±0.02
BaO	0.04±0.03
CO_2	53.36±1.66

804

805

806

807

808

809

810

811

812

813

814

815

816 Tab. 2 Experimental results determined by electron microprobe analyses for
817 each multi-anvil run. The last six experiments in the list are performed in the
818 superliquidus field and result in pokrovskite plus melt. They are plotted in the
819 superliquidus field with the bulk composition of the starting material. The
820 experiments MA465 and MA468 were performed in the subsolidus field and
821 are plotted in Fig. 8b with their bulk compositions.

Sample	Temperature (°C)	Bulk composition	Melt composition	Solid composition
MA449	1600	$Mg_{0.95}Ca_{0.05}CO_3$	$Mg_{0.89(3)}Ca_{0.11}CO_3$	$Mg_{0.98}Ca_{0.02}CO_3$
MA447	1475	$Mg_{0.90}Ca_{0.10}CO_3$	$Mg_{0.75(3)}Ca_{0.25}CO_3$	$Mg_{0.95}Ca_{0.05}CO_3$
MA436	1460	$Mg_{0.85}Ca_{0.15}CO_3$	$Mg_{0.68(3)}Ca_{0.39}CO_3$	$Mg_{0.93}Ca_{0.07}CO_3$
MA446	1400	$Mg_{0.85}Ca_{0.15}CO_3$	$Mg_{0.52(1)}Ca_{0.48}CO_3$	$Mg_{0.90}Ca_{0.10}CO_3$
MA503	1350	$Mg_{0.85}Ca_{0.20}CO_3$	$Mg_{0.40(1)}Ca_{0.60}CO_3$	$Mg_{0.90}Ca_{0.10}CO_3$
MA511	1300	$Mg_{0.75}Ca_{0.25}CO_3$	$Mg_{0.37(1)}Ca_{0.63}CO_3$	$Mg_{0.58(2)}Ca_{0.42}CO_3$; $Mg_{0.85(1)}Ca_{0.15}CO_3$
MA516	1400	$Mg_{0.20}Ca_{0.80}CO_3$	$Mg_{0.20(3)}Ca_{0.80}CO_3$	$Mg_{0.10}Ca_{0.90}CO_3$
MA517	1350	$Mg_{0.20}Ca_{0.80}CO_3$	$Mg_{0.27(3)}Ca_{0.73}CO_3$	$Mg_{0.14}Ca_{0.86}CO_3$
MA513	1575	$Mg_{0.05}Ca_{0.95}CO_3$	$Mg_{0.95}Ca_{0.05}CO_3$	-
MA515	1620	$Mg_{0.05}Ca_{0.95}CO_3$	$Mg_{0.95}Ca_{0.05}CO_3$	-
MA403	1430	$Mg_{0.80}Ca_{0.20}CO_3$; 18 wt.% H_2O	$Mg_{0.83(4)}Ca_{0.17}CO_3$	$Mg_{0.99}Ca_{0.01}CO_3$
MA405	1420	$Mg_{0.80}Ca_{0.20}CO_3$; 18 wt.% H_2O	$Mg_{0.81(5)}Ca_{0.19}CO_3$	$Mg_{0.99}Ca_{0.01}CO_3$
MA435	1400	$Mg_{0.80}Ca_{0.20}CO_3$; 18 wt.% H_2O	$Mg_{0.82(6)}Ca_{0.01}CO_3$	$Mg_{0.99}Ca_{0.01}CO_3$
MA434	1200	$Mg_{0.80}Ca_{0.20}CO_3$; 18 wt.% H_2O	$Mg_{0.47(3)}Ca_{0.01}CO_3$	$Mg_{0.92}Ca_{0.08}CO_3$
MA465	1500	$MgCO_3$; 23 wt.% H_2O	-	$MgCO_3$
MA468	1550	$MgCO_3$; 23 wt.% H_2O	-	$MgCO_3$
MA418	1375	$Mg_{0.80}Ca_{0.20}CO_3$; 18 wt.% H_2O	-	-
MA429	1375	$Mg_{0.80}Ca_{0.20}CO_3$; 18 wt.% H_2O	-	-
MA421	1460	$Mg_{0.87}Ca_{0.13}CO_3$; 20 wt.% H_2O	-	-
MA452	1480	$Mg_{0.91}Ca_{0.09}CO_3$; 20 wt.% H_2O	-	-
MA423	1500	$Mg_{0.93}Ca_{0.07}CO_3$; 21 wt.% H_2O	-	-
MA428	1550	$Mg_{0.93}Ca_{0.07}CO_3$; 21 wt.% H_2O	-	-

822

823

824

825

826 Tab. 3 Results of the falling sphere/body experiments with either
827 hydromagnesite (HM) as starting material or magnesite (M). In experiments
828 MA430 and MA432 the temperature was calculated using the power curve
829 calibration (C).

Sample	Material	Temperature (°C)	Remarks
MA413	HM	1700	no melting
MA430	HM	1743 (C)	no melting
MA431	HM	1746 (C)	melting
MA437	M	1800	melting
MA440	M	1750	no melting
MA507	M	1800	melting

830

831

832

833 Tab. 4 Observed hkl with electron diffraction with the corresponding d-spacing
834 compared to the data from Perchiazzi and Merlino (2006). Observed angles
835 between the lattice planes compared to the data from Perchiazzi and Merlino
836 (2006).

Lattice parameter	Observed	Calculated after Perchiazzi and Merlino (2006)
d_{100} [Å]	12.035	12.0613
d_{040} [Å]	2.559	2.3413
d_{140} [Å]	2.500	2.2456
∡140/100 [°]	77.5	79.12
∡140/400 [°]	12.0	10.88

837

838

839

840 Tab. 5 Average composition of the carbonate melt phase of hydrous samples
841 MA403 and MA405. The compositions were determined either with the help of
842 elemental mappings or averaging several defocused electron beam
843 measurements.

Sample	Method	Magnesite [mole %]	Calacite [mole %]
MA403	mapping	85	15
	defocused beam	83(4)	17
MA405	mapping	79	21
	defocused beam	81(5)	19

844

845

846

847

848

849

850